An Alternative Approach to Nonhydrostatic Modeling

Z. I. JANJIC AND J. P. GERRITY JR.

NCEP/EMC, Camp Springs, Maryland

S. NICKOVIC

ICoD, University of Malta, Valetta, Malta

(Manuscript received 25 February 2000, in final form 12 September 2000)

ABSTRACT

An alternative approach to the design of nonhydrostatic numerical weather prediction (NWP) models is presented. Instead of extending mesoscale nonhydrostatic modeling concepts to the synoptic scales and beyond, a hydrostatic NWP model using the mass-based σ vertical coordinate has been extended to include the nonhydrostatic motions, preserving the favorable features of the hydrostatic formulation. In order to do so, the system of nonhydrostatic equations was split into two parts: (a) the part that corresponds to the hydrostatic system, except for higher-order corrections due to the vertical acceleration, and (b) the system of equations that allows computation of the corrections appearing in the first system due to the vertical acceleration. This procedure does not require any linearization or approximation.

With this approach, the nonhydrostatic dynamics has been introduced through an add-on nonhydrostatic module. The separation of the nonhydrostatic contributions shows in a transparent way where, how, and to what extent relaxing the hydrostatic approximation affects the hydrostatic equations. The nonhydrostatic module can be turned on and off depending on resolution, so that the model can be run in the hydrostatic mode at lower resolutions with no extra cost. This also allows easy comparison of hydrostatic and nonhydrostatic solutions obtained using otherwise identical model.

The nonhydrostatic model developed appears to be computationally robust at all resolutions and efficient in NWP applications. With the current coding, the extra computational effort needed due to the nonhydrostatic extension is of the order of 20% of that required by the hydrostatic dynamics, both in terms of computer time and memory. Compared to the hydrostatic version of the model, no additional computational boundary conditions are needed in real data runs.

At lower resolutions, in the hydrostatic limit, the forecasts of traditional meteorological parameters obtained using the hydrostatic and the nonhydrostatic modes are almost indistinguishable. The model also demonstrated the presence of important two-dimensional nonhydrostatic effects at very high horizontal resolutions. At these scales, the nonhydrostatic model was generally more robust than the hydrostatic one and produced smoother solutions.

The impact of the nonhydrostatic dynamics appears to be weak at the horizontal resolutions of about 8 km. However, a visible effect on the orographic precipitation was detected. In addition to that, the nonhydrostatic deviation of pressure made a significant small-scale contribution to the pressure gradient force at places.

The proposed approach appears well suited for models designed for a wide range of horizontal resolutions, and in particular for unified global and regional forecasting systems. Being developed from an existing model, the new model requires only minimal changes to the existing preprocessing and postprocessing infrastructure.

1. Introduction

Weather forecasting models have reached, or will shortly reach, horizontal resolutions that allow the representation of processes for which the hydrostatic approximation ceases to be valid. For this reason, the formulation and/or implementation of nonhydrostatic numerical weather prediction (NWP) models is considered a matter of priority at many meteorological services and research institutions.

Hydrostatic NWP models evolved over the past four decades and have achieved a high level of reliability and accuracy. Even though claims that optimum model configurations have been reached cannot be supported by rigorous scientific arguments, the vast engineering efforts involved appear to have converged toward several common characteristics shared by the dynamical parts of most major weather forecasting and climate simulation models.

Within the mesoscale modeling community, considerable experience has been accumulated in the formu-

Corresponding author address: Zavisa I. Janjic, NCEP, WWB, Rm. 207, 5200 Auth Road, Camp Springs, MD 20746.
E-mail: wd20zj@ncep.noaa.gov

lation and application of nonhydrostatic models, particularly on cloud or single storm scales. Yet this experience may not be directly applicable in its entirety to NWP, which is dealing with the motions on a much wider range of temporal and spatial scales. Difficulties that may not be significant, or may go unnoticed on the mesoscale, could spoil a nonhydrostatic forecast on the synoptic scale. For example, the conservation of mass is not a matter of much concern at the mesoscale. Yet an erratic gain or loss of mass from case to case would be hard to tolerate in an operational environment where the absence of such errors with the highly evolved hydrostatic models is taken for granted. Another problem may arise concerning the need to control spurious motions generated in upper levels by the nonhydrostatic model dynamics and numerics. Time-dependent computational top boundary conditions that could control this problem could further limit the capacity of a regional nonhydrostatic model to develop more accurate synoptic-scale forecasts than the parent hydrostatic model. Finally, there is insufficient experience concerning the benefits that can be expected in NWP from nonhydrostatic models.

For these reasons, the first priority appears to be that a nonhydrostatic NWP model gives solutions that at least are not inferior to solutions of a good hydrostatic model in the range of validity of the hydrostatic approximation. Of course, the model should also be able to reproduce important nonhydrostatic motions at very high resolutions. Although such resolutions may not be affordable for NWP applications in the near future, and therefore may not be relevant for NWP, this condition must be satisfied in order to demonstrate the soundness of the formulation. Another obvious requirement is that the extra computational cost due to the more complex nonhydrostatic dynamics be affordable. This becomes even more important considering the uncertainty of the benefits that will accrue from the nonhydrostatic formulation.

Most NWP and climate hydrostatic models use hydrostatic pressure, or mass-based vertical coordinates, which, almost automatically, guarantee the mass conservation. On the other hand, most mesoscale models, including those intended for NWP applications, use the geometrical height as the basis for their vertical coordinates. Attempts to use hydrostatic pressure as the vertical coordinate in nonhydrostatic models have also been made. Recently, Bubnova et al. (1995) reported a successful application of the hydrostatic coordinate in a limited area spectral model following Laprise (1992).

Having in mind the stated criteria, a new approach is proposed as an alternative to the usual practice of extending mesoscale nonhydrostatic concepts to the synoptic scales. This approach is based on relaxing the hydrostatic approximation in a mass-based σ coordinate hydrostatic model, thereby extending the applicability of the model to the nonhydrostatic motions. In order to do so, the system of nonhydrostatic equations is split into two parts: (a) the part that corresponds to the hydrostatic system, except for higher-order corrections due to the vertical acceleration, and (b) the system of equations that allows computation of the corrections appearing in the first system due to the vertical acceleration. This procedure does not require any linearization or approximation. With this, evolutionary, approach, the favorable features of the hydrostatic model are preserved within the range of validity of the hydrostatic approximation.

Following the described strategy, the nonhydrostatic dynamics is introduced through an add-on module. The separation of the nonhydrostatic contributions shows in a transparent way where, how, and to what extent relaxing the hydrostatic approximation affects the hydrostatic equations. The nonhydrostatic module can be turned on and off depending on resolution, so that the model can be run in the hydrostatic mode at lower resolutions with no extra cost. This also allows easy comparison of hydrostatic and nonhydrostatic solutions obtained using otherwise identical models.

2. Nonhydrostatic model equations

Following Laprise (1992), the symbol π will represent the hydrostatic pressure. The generalized vertical coordinate σ is defined in terms of the hydrostatic pressure by the expression

$$\sigma = (\pi - \pi_t)/(\pi_s - \pi_t), \tag{2.1}$$

wherein π_s and π_t stand for the hydrostatic pressures at the surface and at the top of the model atmosphere. Let μ represent the difference in hydrostatic pressure between the base and top of the model column; that is, $\mu = \pi_s - \pi_t$. It is assumed that π_t is a positive constant, whereas π_s is a function of time and horizontal position.

Assume that a box with cross section S contains mass of the air M with the density ρ. Then,

$$Mg = \mu\Delta\sigma S = g\rho S\Delta z, \tag{2.2}$$

where g is gravity and Δz is the height of the box. The hypsometric equation that relates the geopotential Φ to the hydrostatic pressure,

$$\frac{\partial\Phi}{\partial\sigma} = -\alpha\mu, \tag{2.3}$$

is readily obtained from (2.2). In (2.3), α is the specific volume. Using the definitions of σ and μ, (2.3) may be rewritten as

$$\frac{\partial\Phi}{\partial\pi} = -\alpha. \tag{2.4}$$

Assuming that the atmosphere is dry, the specific volume is related to the temperature T and pressure p by the ideal gas law: $\alpha = RT/p$, R being the gas constant. Note that the ideal gas law does not involve the hydro-

static pressure but rather the actual pressure. Using the ideal gas law, from (2.3),

$$\frac{\partial \Phi}{\partial \sigma} = -\mu \frac{RT}{p}. \tag{2.5}$$

Upon integration of (2.5) from the surface, where the geopotential is denoted by Φ_s, to an arbitrary level σ,

$$\Phi = \Phi_s + \mu \int_\sigma^1 \frac{RT}{p}\, d\sigma. \tag{2.6}$$

Using (2.4), the third equation of motion may be written as

$$\frac{dw}{dt} = g\left(\frac{\partial p}{\partial \pi} - 1\right). \tag{2.7}$$

Defining the ratio of the vertical acceleration and gravity g,

$$\varepsilon \equiv \frac{1}{g}\frac{dw}{dt}, \tag{2.8}$$

(2.7) may be rewritten as

$$\frac{\partial p}{\partial \pi} = 1 + \varepsilon, \tag{2.9}$$

which defines the relationship between the hydrostatic and the nonhydrostatic pressures. Integrating (2.9) with respect to π, one obtains the nonhydrostatic pressure at an arbitrary hydrostatic pressure or σ level, that is,

$$p = \int_{\pi_t}^{\pi} \frac{\partial p}{\partial \pi'}\, d\pi' = \int_0^\sigma (1 + \varepsilon)\mu\, d\sigma'. \tag{2.10}$$

As can be seen from (2.9) and (2.10), should ε vanish, the pressure and the hydrostatic pressure become equivalent.

In the hydrostatic σ coordinate system, the time derivative of a fluid property q following the motion of an air parcel may be written as

$$\frac{dq}{dt} = \frac{\partial q}{\partial t} + \mathbf{v}\cdot\nabla_\sigma q + \dot\sigma \frac{\partial q}{\partial \sigma}. \tag{2.11}$$

Here, $\dot\sigma$ is the vertical velocity.

The conservation of mass may be expressed by

$$w = \frac{1}{g}\left(\frac{\partial \Phi}{\partial t} + \mathbf{v}\cdot\nabla_\sigma \Phi + \dot\sigma \frac{\partial \Phi}{\partial \sigma}\right), \tag{2.12}$$

and, if μ is substituted for $\partial\pi/\partial\sigma$, by

$$\frac{d\mu}{dt} + \mu\left(\nabla_\sigma\cdot\mathbf{v} + \frac{\partial \dot\sigma}{\partial \sigma}\right) = 0. \tag{2.13}$$

Equation (2.12) may be regarded as a definition of w, the time rate of change of geopotential height following the motion of a fluid parcel. Equation (2.13) is the mass continuity equation in the form used in hydrostatic models.

Using the material surface boundary conditions $\dot\sigma \equiv d\sigma/dt = 0$ at $\sigma = 0$ and $\sigma = 1$, one may obtain two equations from (2.13). The first one gives the tendency of the hydrostatic surface pressure

$$\frac{\partial \mu}{\partial t} = -\int_0^1 \nabla_\sigma\cdot(\mu\mathbf{v})\, d\sigma', \tag{2.14}$$

and the second one is used to calculate the vertical velocity in the σ coordinate system

$$\mu\dot\sigma = -\sigma\frac{\partial \mu}{\partial t} - \int_0^\sigma \nabla_\sigma\cdot(\mu\mathbf{v})\, d\sigma'. \tag{2.15}$$

Using the relations (2.4) and (2.9), in the case of a nonhydrostatic atmosphere one obtains

$$-\frac{1}{\rho}\nabla_z p \equiv -(1 + \varepsilon)\nabla_\sigma\Phi - \alpha\nabla_\sigma p. \tag{2.16}$$

Here the subscripts indicate the variable that is kept constant while the differentiation is performed. Using (2.16), the inviscid nonhydrostatic equation for the horizontal part of the wind takes the form

$$\frac{d\mathbf{v}}{dt} = -(1 + \varepsilon)\nabla_\sigma\Phi - \alpha\nabla_\sigma p + f\mathbf{k}\times\mathbf{v}. \tag{2.17}$$

Again, for vanishing ε, (2.17) reduces to the form used in hydrostatic models.

The first law of thermodynamics for adiabatic processes has the form

$$c_p\frac{dT}{dt} = \alpha\frac{dp}{dt}, \tag{2.18}$$

in which c_p is the specific heat at constant pressure. In hydrostatic models, the derivative dp/dt is replaced by the derivative of hydrostatic pressure $d\pi/dt$, often denoted by the Greek letter omega. For this reason, the right-hand side of the equation is frequently referred to as the omega–alpha term. The derivative of pressure can be separated into a component ω_1 that reduces to the hydrostatic expression when ε vanishes, and a component ω_2 that vanishes with vanishing ε. Note that, generally, $p = p(x, y, \pi, t)$. Then

$$\frac{\partial p}{\partial t} = \frac{\partial p}{\partial \pi_t}\frac{\partial \pi}{\partial t} + \frac{\partial p}{\partial t_\pi} = (1 + \varepsilon)\frac{\partial \pi}{\partial t} + \frac{\partial p}{\partial t_\pi}, \tag{2.19}$$

where the subscripts indicate the variable that is kept constant while the differentiation is performed. In addition to that, as can be seen from (2.9),

$$\dot\sigma\frac{\partial p}{\partial \sigma} = (1 + \varepsilon)\dot\sigma\frac{\partial \pi}{\partial \sigma}. \tag{2.20}$$

Thus, dp/dt is written in the form

$$\frac{dp}{dt} = \omega_1 + \omega_2, \tag{2.21}$$

where

$$\omega_1 \equiv (1 + \varepsilon)\frac{\partial \pi}{\partial t} + \mathbf{v} \cdot \nabla_\sigma p + (1 + \varepsilon)\dot{\sigma}\frac{\partial \pi}{\partial \sigma}, \quad (2.22)$$

or taking into account (2.15) and the fact that $\mu = \partial \pi/\partial \sigma$,

$$\omega_1 = \mathbf{v} \cdot \nabla_\sigma p - (1 + \varepsilon) \int_0^\sigma \nabla_\sigma \cdot (\mu \mathbf{v})\, d\sigma'. \quad (2.23)$$

Note that the contribution of the second term of the pressure gradient force (2.16) to the kinetic energy generation is compensated by the contribution of the horizontal advection of pressure in (2.22). The second part of ω is defined by

$$\omega_2 \equiv \frac{\partial p}{\partial t} - (1 + \varepsilon)\frac{\partial \pi}{\partial t}. \quad (2.24)$$

Starting from (2.13), it can be shown that

$$\omega_2 = \int_0^\sigma \left[\frac{\partial \varepsilon}{\partial t}\frac{\partial (\sigma' \mu)}{\partial \sigma'} - \frac{\partial (\sigma' \mu)}{\partial t}\frac{\partial \varepsilon}{\partial \sigma'}\right] d\sigma'. \quad (2.25)$$

Note that the term (2.24) indeed vanishes for vanishing ε.

In view of the separation of omega into two parts, the thermodynamic equation is separated into two parts as well:

$$\left(\frac{\partial T}{\partial t}\right)_1 = -\mathbf{v} \cdot \nabla_\sigma T - \dot{\sigma}\frac{\partial T}{\partial \sigma} + \frac{1}{c_p}(\alpha \omega_1) \quad \text{and} \quad (2.26)$$

$$\left(\frac{\partial T}{\partial t}\right)_2 = \frac{1}{c_p}(\alpha \omega_2). \quad (2.27)$$

Note that with the aid of (2.23), (2.26) may be rewritten as

$$\left(\frac{\partial T}{\partial t}\right)_1 = -\mathbf{v} \cdot \nabla_\sigma T - \dot{\sigma}\frac{\partial T}{\partial \sigma} + \frac{\alpha}{c_p}\left[\mathbf{v} \cdot \nabla_\sigma p - (1 + \varepsilon) \int_0^\sigma \nabla_\sigma \cdot (\mu \mathbf{v})\, d\sigma'\right]. \quad (2.28)$$

Again, when ε vanishes, (2.26) and (2.28) take the form used in hydrostatic models, and the equation for the second part (2.27) takes the trivial form $(\partial T/\partial t)_2 = 0$.

The nonhydrostatic system of equations is closed by applying the operator (2.11) to the continuity equation (2.12) in order to obtain the vertical acceleration dw/dt. Then, from (2.8),

$$\varepsilon = \frac{1}{g}\frac{dw}{dt} = \frac{1}{g}\left(\frac{\partial w}{\partial t} + \mathbf{v} \cdot \nabla_\sigma w + \dot{\sigma}\frac{\partial w}{\partial \sigma}\right). \quad (2.29)$$

The parameter ε is evidently the central point of the extended, nonhydrostatic dynamics. Assume for a moment that ε is zero. Then, Eqs. (2.4), (2.13), (2.17), and (2.28), together with the gas law, represent the set of equations describing the hydrostatic, inviscid, adiabatic atmosphere. However, the presence of nonzero ε in (2.9), (2.17), and (2.28) demonstrate in a very transparent way where, how, and to what extent relaxing the hydrostatic approximation affects the familiar hydrostatic equations. Note that the system of equations developed above bears a close relation to the system which Laprise (1992) referred to as an ''alternative formulation.'' Therefore, all theoretical considerations of Laprise (1992) apply to this system as well.

On the synoptic scales, ε is very small and approaches the computer round-off error. However, in case of vigorous convective storms, or strong vertical accelerations in the flows over steep obstacles, the vertical velocity can reach the order of 10 m s^{-1} over the period of the order of 1000 s. This yields an estimate of the vertical acceleration of the order of 10^{-2} m s^{-2}, and consequently, ε of the order of 10^{-3}. As can be seen from (2.9), for this value of ε the nonhydrostatic deviation of pressure can reach 100 hPa. Bearing in mind that the typical synoptic-scale horizontal pressure gradient is of the order of 100 hPa over 100 km, this suggests that significant local nonhydrostatic pressure gradients and associated circulations may develop on small scales.

3. Temporal discretization

The numerical model described here uses the equations discussed in the preceding section cast into finite difference form. By using numerical methods that have been successful in hydrostatic models, it is expected that the model will behave well in the hydrostatic limit, that is, when applied with resolutions that do not support significant vertical accelerations.

For vanishing ε, the prognostic equations of the quasi-hydrostatic system of equations, that is, (2.4), (2.13), (2.17), and (2.28), together with the gas law, can be conveniently split into two energy conserving subsystems of prognostic equations, that is,

$$\left(\frac{\partial \mathbf{v}}{\partial t}\right)_{\mathrm{i}} = -\nabla_\sigma \Phi - \alpha \nabla_\sigma \pi + f\mathbf{k} \times \mathbf{v}, \quad (3.1)$$

$$\left(\frac{\partial T}{\partial t}\right)_{\mathrm{i}} = \frac{\alpha}{c_p}\left[\mathbf{v} \cdot \nabla_\sigma \pi - \int_0^\sigma \nabla_\sigma \cdot (\mu \mathbf{v})\, d\sigma'\right], \quad (3.2)$$

$$\frac{\partial \mu}{\partial t} + \nabla_\sigma \cdot (\mu \mathbf{v}) + \frac{\partial (\mu \dot{\sigma})}{\partial \sigma} = 0, \quad (3.3)$$

$$\left(\frac{\partial \mathbf{v}}{\partial t}\right)_{\mathrm{ii}} = -\mathbf{v}\nabla_\sigma \mathbf{v} - \dot{\sigma}\frac{\partial \mathbf{v}}{\partial \sigma}, \quad (3.4)$$

$$\left(\frac{\partial T}{\partial t}\right)_{\mathrm{ii}} = -\mathbf{v} \cdot \nabla_\sigma T - \dot{\sigma}\frac{\partial T}{\partial \sigma}. \quad (3.5)$$

The time derivatives of the two subsystems are denoted

by subscripts i and ii, respectively. As can be readily verified, the system (3.1)–(3.2), together with the continuity equation (2.13) rewritten here in somewhat different form (3.3), conserves energy. The same applies to the system (3.4)–(3.5) combined with the continuity equation that links the two subsystems.

An economical forward–backward scheme (Ames 1969; Gadd 1974) with the trapezoidal scheme for the Coriolis term (Janjic and Wiin-Nielsen 1977) has been successfully applied in a hydrostatic model to the system (3.1)–(3.3) (cf. Janjic 1979). The properties of the scheme used in the model were examined in the case of the linearized shallow water equations [e.g., by Janjic and Wiin-Nielsen (1977) and Janjic (1979)]. Concerning the contributions of the advection terms (3.4)–(3.5), there is a variety of possible choices. For example the split, iterative, first forward then (slightly off) centered time differencing scheme (cf. Janjic 1979) has been successfully used in synoptic-scale models with time steps twice longer than those used to solve the subsystem (3.1)–(3.3) (Janjic et al. 1995). In the formulation discussed here, this two-step iterative scheme has been replaced by the Adams–Bashforth scheme, and the directional splitting has been eliminated. The Adams–Bashforth scheme allows the same computational efficiency as the two-step, iterative scheme, and the accuracy is improved by reducing or avoiding the effects of splitting. However, somewhat more memory is needed in order to store some of the variables at the third time level, and the physical mode of the Adams–Bashforth scheme is weakly unstable. As experience shows, this instability can be tolerated if the time steps are not too long. Note that large ratios between the advection time step and the time step used for the remaining terms of the equations cannot be used in NWP applications. Namely, since the wind speed can exceed 100 m s^{-1}, this ratio is restricted to 2 or 3, at most.

The described time differencing schemes are applied to the system (2.13), (2.17), and (2.28). However, certain extensions are needed in order to compute ε. These extensions will be described here and analyzed in more detail in the next section.

The superscripts n and $n + 1$ will be used to denote the time levels for all variables, with the exception of the vertical velocity w, which is defined at the intermediate time levels indicated by superscripts $n + ½$ or $n - ½$. The superscript $n + ½$ will be used also in the advection terms in order to indicate the terms extrapolated in time in the Adams–Bashforth procedure. Because the nonhydrostatic equations have been separated into two components, similar to the previous section, the subscript 1 will be used to indicate that a variable has been advanced in time only by the first component equation. For example, the solution of (2.28) starting from the time level n will be denoted by the subscript 1, since (2.27) remains to be solved before reaching the time level $n + 1$.

As usual, the vertical velocity in the hydrostatic sigma coordinate is computed from

$$\dot{\sigma}^n = \frac{\sigma \int_0^1 \nabla_\sigma \cdot (\mu^n \mathbf{v}^n)\, d\sigma' - \int_0^\sigma \nabla_\sigma \cdot (\mu^n \mathbf{v}^n)\, d\sigma'}{\mu^n}, \quad (3.6)$$

and the surface pressure tendency equation is

$$\mu^{n+1} = \mu^n - \Delta t \int_0^1 \nabla_\sigma \cdot (\mu^n \mathbf{v}^n)\, d\sigma'. \quad (3.7)$$

From the solution for μ^{n+1}, one readily obtains

$$p_1 = p^n + \sigma(1 + \varepsilon^n)(\mu^{n+1} - \mu^n), \quad \text{and} \quad (3.8)$$

$$\omega_1 = \mathbf{v}^n \cdot \nabla_\sigma p^n - (1 + \varepsilon^n) \int_0^\sigma \nabla_\sigma \cdot (\mu^n \mathbf{v}^n)\, d\sigma'. \quad (3.9)$$

The first component of the thermodynamic equation is then

$$T_1^* = T^n + \frac{\Delta t}{c_p} \frac{RT^n}{p^n} \omega_1, \quad (3.10)$$

and after adding the Adams–Bashforth advection,

$$T_1 = T_1^* - \Delta t \left(\mathbf{v}^n \cdot \nabla_\sigma T_1^{n+1/2*} - \dot{\sigma}^n \frac{\partial T_1^{n+1/2*}}{\partial \sigma} \right). \quad (3.11)$$

The superscript $n + ½$ in the advection terms indicates symbolically the extrapolation in time for half the time step forward involved in the Adams–Bashforth procedure. In the actual algorithm, the values denoted by the superscript $n + ½*$ and the subscript 1 are obtained using the current T_1^* and one time step old T_1^*.

The second component of the thermodynamic equation is

$$T^{n+1} - T_1 = \frac{1}{c_p} \frac{RT_1}{p_1} (p^{n+1} - p_1). \quad (3.12)$$

The hypsometric equation yields the geopotential associated with the first component solutions for temperature and pressure,

$$\Phi_1 = \Phi_s + \mu^{n+1} \int_\sigma^1 \frac{RT_1}{p_1}\, d\sigma', \quad (3.13)$$

and the second component equation yields

$$\Phi^{n+1} = \Phi_s + \mu^{n+1} \int_\sigma^1 \frac{RT^{n+1}}{p^{n+1}}\, d\sigma'. \quad (3.14)$$

The value of vertical velocity w associated with the first component solutions is obtained from

$$gw_1 = \frac{\Phi_1 - \Phi^n}{\Delta t} + \mathbf{v}^n \cdot \nabla_\sigma \Phi_1 + \dot{\sigma}^n \frac{\partial \Phi_1}{\partial \sigma}. \quad (3.15)$$

Note that Φ_1 is an intermediate value of geopotential between Φ^n and Φ^{n+1}, that is,

$$\Phi^{n+1} - \Phi_1 \le O(\Delta t). \tag{3.16}$$

Therefore, using Φ_1 in the advection terms of (3.15) in order to compute w is a consistent numerical approximation. On the other hand, neglecting the contribution $(\Phi^{n+1} - \Phi_1)/\Delta t$ would be wrong in view of (3.16). Thus,

$$w^{n+1/2} - w_1 = \frac{\Phi^{n+1} - \Phi_1}{g\Delta t}, \tag{3.17}$$

which must also satisfy the third equation of motion,

$$w^{n+1/2} - \frac{g\Delta t}{\mu^{n+1}}\frac{\partial p^{n+1}}{\partial \sigma} = w_1 - g\Delta t(1 + \varepsilon_1). \tag{3.18}$$

The value of ε associated with the first component solutions is obtained from

$$g\varepsilon_1 = \frac{w_1 - w^n}{\Delta t} + \mathbf{v}^n \cdot \nabla_\sigma w_1 + \dot{\sigma}^n \frac{\partial w_1}{\partial \sigma}, \tag{3.19}$$

and the second component from

$$\varepsilon^{n+1} = \frac{1}{\mu^{n+1}}\frac{\partial p^{n+1}}{\partial \sigma} - 1. \tag{3.20}$$

Upon solution of the preceding equations for thermodynamic variables, the pressure gradient force at the time level $n + 1$ can be computed, and the horizontal equation of motion can be used to advance the wind components in time. The Adams–Bashforth scheme is used to compute the contribution of the advection terms,

$$\mathbf{v}^{n+1*} = \mathbf{v}^n - \Delta t\left(\mathbf{v}^n \cdot \nabla_\sigma \mathbf{v}^{n+1/2} + \dot{\sigma}^n \frac{\partial \mathbf{v}^{n+1/2}}{\partial \sigma}\right), \tag{3.21}$$

and then the backward scheme for the pressure gradient force term, and the trapezoidal scheme for the Coriolis term, are used to complete the step

$$\mathbf{v}^{n+1} = \mathbf{v}^{n+1*} - \Delta t\left[(1 + \varepsilon^{n+1})\nabla_\sigma \Phi^{n+1} - \alpha^{n+1}\nabla_\sigma p^{n+1} + f\mathbf{k} \times \frac{(\mathbf{v}^{n+1*} + \mathbf{v}^{n+1})}{2}\right]. \tag{3.22}$$

Here, the specific volume α^{n+1} is

$$\alpha^{n+1} = \frac{RT^{n+1}}{p^{n+1}}. \tag{3.23}$$

4. Solution of the coupled equations

Equations (3.12), (3.14), (3.17), and (3.18) are coupled equations. Their solution will be sought by eliminating all unknowns except p^{n+1}, solving the resulting equation, and then back-substituting to obtain T^{n+1}, Φ^{n+1}, $w^{n+1/2}$, and ε^{n+1}. Namely, (3.13) and (3.14), together with (3.17) and (3.18), can be combined to give

$$R\mu^{n+1}\int_\sigma^1 \left(\frac{T^{n+1}}{p^{n+1}} - \frac{T_1}{p_1}\right) d\sigma' = (g\Delta t)^2\left[\frac{1}{\mu^{n+1}}\frac{\partial p^{n+1}}{\partial \sigma} - (1 + \varepsilon_1)\right]. \tag{4.1}$$

Using (3.12) to eliminate T^{n+1}, (4.1) may be rewritten as

$$R(1 - \kappa)\mu^{n+1}\int_\sigma^1 T_1\left(\frac{1}{p^{n+1}} - \frac{1}{p_1}\right) d\sigma' = (g\Delta t)^2\left[\frac{1}{\mu^{n+1}}\frac{\partial p^{n+1}}{\partial \sigma} - (1 + \varepsilon_1)\right], \tag{4.2}$$

where $\kappa \equiv R/c_p$. Define a pressure p^* that satisfies the equation

$$\frac{\partial p^*}{\partial \sigma} \equiv \mu^{n+1}(1 + \varepsilon_1), \tag{4.3}$$

subject to the boundary condition $p^* = \pi_t$ at $\sigma = 0$. Upon inserting (4.3) into (4.2), one obtains

$$\frac{R(1 - \kappa)}{g^2}\int_\sigma^1 T_1\left(\frac{\mu^{n+1}}{p^{n+1}} - \frac{\mu^{n+1}}{p_1}\right) d\sigma' = \Delta t^2 \frac{\partial\left(\dfrac{p^{n+1}}{\mu^{n+1}} - \dfrac{p^*}{\mu^{n+1}}\right)}{\partial \sigma}. \tag{4.4}$$

Note that

$$\frac{p^{n+1}}{\mu^{n+1}} - \frac{p^*}{\mu^{n+1}} \le O(\Delta t), \tag{4.5}$$

so that, from (4.4),

$$\frac{R(1 - \kappa)}{g^2}\int_\sigma^1 T_1\left(\frac{\mu^{n+1}}{p^{n+1}} - \frac{\mu^{n+1}}{p_1}\right) d\sigma' \le O(\Delta t^3), \tag{4.6}$$

which illustrates how subtle is the difference between p_1 and p^{n+1}.

Differentiating (4.4) with respect to σ, introducing the definitions

$$\psi \equiv \frac{p^{n+1}}{\mu^{n+1}}, \qquad \psi^* \equiv \frac{p^*}{\mu^{n+1}}, \qquad \psi_1 \equiv \frac{p_1}{\mu^{n+1}},$$
$$\Gamma \equiv (1 - \kappa)\frac{RT_1}{(g\Delta t)^2} \tag{4.7}$$

and rearranging the resulting equation, one obtains

$$\frac{\partial^2(\psi - \psi^*)}{\partial \sigma^2} + \Gamma\frac{\psi_1 - \psi}{\psi_1 \psi} = 0. \tag{4.8}$$

Finally, define

$$\chi \equiv \psi - \psi^*, \qquad D \equiv \psi_1 - \psi^*, \quad \text{and}$$
$$\overline{\psi}(\sigma) \equiv \psi_1(\sigma) + \kappa\left[\overline{\psi}(\sigma - d\sigma) + \frac{\partial \psi_1}{\partial \sigma}d\sigma - \psi_1(\sigma)\right]. \tag{4.9}$$

The product $\psi_1\psi$ that appears in the denominator of the undifferentiated term in (4.8) may be approximated by $\overline{\psi}^2$. Letting $\gamma^2 \equiv \Gamma/\overline{\psi}^2$, (4.8) can then be rewritten as

$$\frac{\partial^2\chi}{\partial\sigma^2} - \gamma^2\chi = -\gamma^2 D. \tag{4.10}$$

This equation can be solved, for example, by iterative relaxation subject to the specification of appropriate boundary conditions. A suitable first guess for the iteration is $\chi = \overline{\psi} - \psi^*$. Note that instead of using $\overline{\psi}^2$ in (4.12), the product $\psi_1\psi$ could have been retained in the iterative process. Concerning the accuracy, however, this appears meaningless in view of (4.6).

In order to address the problem of specification of appropriate boundary conditions for (4.10), consider a horizontally homogenous atmosphere at rest and in hydrostatic equilibrium. Let the equations be linearized around such a basic state. Also, consider only the solutions that preserve the horizontal homogeneity. As can be readily verified, the requirement for the horizontal homogeneity eliminates all motions that belong to the first part of the time stepping procedure. In other words, the intermediate solutions denoted by subscript 1 will coincide with the initial values denoted by superscript *n*. The only solutions left will be those described by the linearized set of coupled equations leading to (4.10). In particular, from (3.12),

$$(T^{n+1} - T_0) - (T^n - T_0) = \frac{1}{c_p}\frac{RT_0}{\pi_0}[(p^{n+1} - \pi_0) - (p^n - \pi_0)], \tag{4.11}$$

and after differentiation of (3.14) with respect to σ, linearization, and rearrangement,

$$g\frac{\partial(z^{n+1} - z_0)}{\partial\pi_0} = -\frac{R(T^{n+1} - T_0)}{\pi_0} + \frac{RT_0}{\pi_0}\frac{(p^{n+1} - \pi_0)}{\pi_0}. \tag{4.12}$$

Here, z is the height and subscript 0 denotes the basic-state variables. From (3.17) and (3.18)

$$w^{n+1/2} = \frac{(z^{n+1} - z_0) - (z^n - z_0)}{\Delta t}, \tag{4.13}$$

$$\frac{w^{n+1/2} - w^{n-1/2}}{\Delta t} = g\frac{\partial(p^{n+1} - \pi_0)}{\partial\pi_0}. \tag{4.14}$$

Introducing primes to denote the deviations from the basic state, applying the simplest time differencing operator to (4.12) and using (4.13),

$$g\frac{\partial w^{n+1/2}}{\partial\pi_0} = -\frac{R(T'^{n+1} - T'^n)}{\pi_0\Delta t} + \frac{RT_0}{\pi_0}\frac{(p'^{n+1} - p'^n)}{\pi_0\Delta t}. \tag{4.15}$$

Using (4.11) to eliminate T' in (4.15), and differencing in time the resulting equation, one obtains

$$g\frac{\partial}{\partial\pi_0}\frac{w^{n+1/2} - w^{n-1/2}}{\Delta t} = \frac{c_v}{c_p}\frac{RT_0}{\pi_0^2}\frac{(p'^{n+1} - 2p'^n + p'^{n-1})}{\Delta t^2}. \tag{4.16}$$

On the other hand, differentiating (4.14) with respect to π_0,

$$\frac{\partial}{\partial\pi_0}\frac{w^{n+1/2} - w^{n+1/2}}{\Delta t} = g\frac{\partial^2 p'^{n+1}}{\partial\pi_0^2}. \tag{4.17}$$

Thus, combining (4.16) and (4.17), and taking into account that the basic state is hydrostatic,

$$\frac{(p'^{n+1} - 2p'^n + p'^{n-1})}{\Delta t^2} = \frac{c_p}{c_v}RT_0\frac{\partial^2 p'^{n+1}}{\partial z_0^2}. \tag{4.18}$$

The equation for vertically propagating sound waves is readily recognized in (4.18), although finite differencing is used instead of differentiation with respect to time on the left-hand side.

Now that the physical nature of the processes involved in the second part of the integration procedure have been revealed, the question of the boundary conditions for (4.10) can be readdressed. It appears natural to keep the upper end of the oscillator described by (4.18) fixed, and the lower end free. Thus, χ is set to zero at $\sigma = 0$, and $\partial\chi/\partial\sigma = 0$ at $\sigma = 1$. Such an upper boundary condition is perfectly justified for vanishing pressure at the top of the atmosphere of the model.

5. The nonhydrostatic limit

The tests discussed in this section deal with small-scale buoyancy driven flows and disturbances of uniform flow induced by small orographic obstacles. Such problems are typically studied in two dimensions, that is, in the vertical plane.

In contrast to the flow regimes typically encountered in NWP, the flow on the small scales is not quasi horizontal; it is very divergent, very nonlinear, and very dissipative. The numerical solutions in these flow regimes are sensitive to the specification of the boundary conditions and the intensity and nature of the damping techniques used. In addition to that, typically thousands, or tens of thousands, of time steps are made. Thus, the numerical solutions are likely to develop the nonlinear instability. An effective method for controlling the nonlinear instability on these scales is either damping implied in the numerical algorithm (historically very popular in computational hydrodynamics other than NWP), or explicit artificial damping or filtering if the conservative spatial differencing is chosen.

Another typical difference between the limited area NWP models and the two-dimensional models for simulating small-scale flows is the treatment of the lateral boundary conditions. In the limited area NWP models, the lateral boundary conditions are typically overspecified as required by the centered finite differences. However, zones of increased damping, filtering, or

blending along the boundaries are usually used in order to control the inconsistencies between the model solution inside the integration domain and at the boundaries (cf. Davies 1976). In contrast to that, radiative lateral boundary conditions are usually applied in the two-dimensional nonhydrostatic models.

Within this study, a two-dimensional model was developed in order to test the ideas exposed in the preceding sections. As usual for these scales, the Coriolis force is neglected. Since there is no implied dissipation in the numerical schemes, following the usual practice, artificial damping kept to a necessary minimum is used in order to control the nonlinear instability. The cyclic lateral boundary conditions are prescribed. However, in order to reduce the interference with the recurring periodic solutions, in some of the tests, the Rayleigh damping was applied along the lateral boundaries. Otherwise, the dynamics and numerics of the two-dimensional model are as close as possible to those of the three-dimensional model that will be used for real data tests in the next section.

The processes discussed in this section require horizontal and vertical resolutions of the order of few hundred meters. These processes are not, and most likely will not be, resolved in NWP applications in foreseeable future. For this reason, the objective of the tests presented here is only to demonstrate, even qualitatively, that the important nonhydrostatic motions are present in the proposed model formulation. The study of these processes is beyond the scope of this paper.

a. The cold bubble test

Following Straka et al. (1993), in a neutrally stratified atmosphere with the potential temperature of 300 K, an initial cold disturbance of the form

$$T(x, z) = \overline{T}(x, z) - 15 \cos^2\left[\frac{\pi}{2}\sqrt{\left(\frac{x - x_c}{x_t}\right)^2 + \left(\frac{z - z_c}{z_t}\right)^2}\right], \quad \text{if } \sqrt{\left(\frac{x - x_c}{x_t}\right)^2 + \left(\frac{z - z_c}{z_t}\right)^2} \le 1 \qquad (5.1)$$

was introduced, where

$$x_c = 0 \text{ m}, \quad z_c = 3000 \text{ m}, \quad x_t = 4000 \text{ m}, \quad z_t = 2000 \text{ m}. \qquad (5.2)$$

The integration domain extended 40 km in the x direction, and the free surface was located at 442 hPa, that is, at about 6400 m. The center of the initial disturbance was in the middle of the domain in the x direction, that is, 20 km away from either of the lateral boundaries. As in the main test in the Straka et al. (1993) study, the horizontal resolution was 100 m, and the vertical resolution was 100 m on the average. The time step was 0.3 s, which was proportionally considerably longer than the time steps used in the tests described by Straka et al (1993). There was no divergence damping or Rayleigh damping. However, as in the tests reported in Straka et al. (1993), second-order diffusion was applied in both horizontal and vertical directions with the diffusion coefficient $K = 75 \text{ m}^2 \text{ s}^{-1}$. In addition to that, a centered three-point spatial filter with the coefficient wa = 0.15 was applied to ε_1 defined by (3.19). As demonstrated by numerical tests (not shown), the amount of damping introduced by this filter is negligible. In contrast to the tests discussed by Straka et al. (1993), no time filtering was used.

The potential temperatures after 300, 600, and 900 s are displayed in Fig. 1. The area shown in the figure extends from the center of the domain to 19 200 m to the right, and from the surface to 4600 m. The contour interval is 1 K. The u component of the wind (upper panel) and the w component of the wind (lower panel) after 900 s are shown in the same arrangement in Fig. 2. The dashed contours indicate negative values. The contour interval is 2 m s^{-1}. Comparison of Figs. 1 and 2 with the Straka et al. (1993) converged reference solution reveals very reasonable quantitative and qualitative agreement.

An already mentioned advantage of the current approach is that solutions of the exact hydrostatic counterpart of the model can be studied. The hydrostatic model was unable to reproduce the results shown in Figs. 1 and 2. The hydrostatic solution was computationally unstable unless the lateral diffusion was increased by an order of magnitude. In that case, however, only very crude, qualitative resemblance to the nonhydrostatic solution was preserved.

b. The warm bubble test

Following Drogemeier (1985), and Gallus and Rancic (1996), in a neutral atmosphere with the potential temperature of 300 K, an initial disturbance of the potential temperature

$$\theta(x, z) = \overline{\theta}(x, z) + 6.6 \cos^2\left[\frac{\pi}{2}\sqrt{\left(\frac{x - x_c}{x_t}\right)^2 + \left(\frac{z - z_c}{z_t}\right)^2}\right], \quad \text{if } \sqrt{\left(\frac{x - x_c}{x_t}\right)^2 + \left(\frac{z - z_c}{z_t}\right)^2} \le 1 \qquad (5.3)$$

was introduced, where

$$x_c = 0 \text{ m}, \quad z_c = 2750 \text{ m}, \quad x_t = 2500 \text{ m}, \quad z_t = 2500 \text{ m}. \qquad (5.4)$$

The integration domain extended 20 km in the x direction. The free surface was located at 135 hPa, that is, at about 13 500 m. The center of the initial disturbance was in the middle of the domain in the x direction, that is, 10 km away from either of the lateral boundaries. The horizontal resolution was 100 m, and the vertical

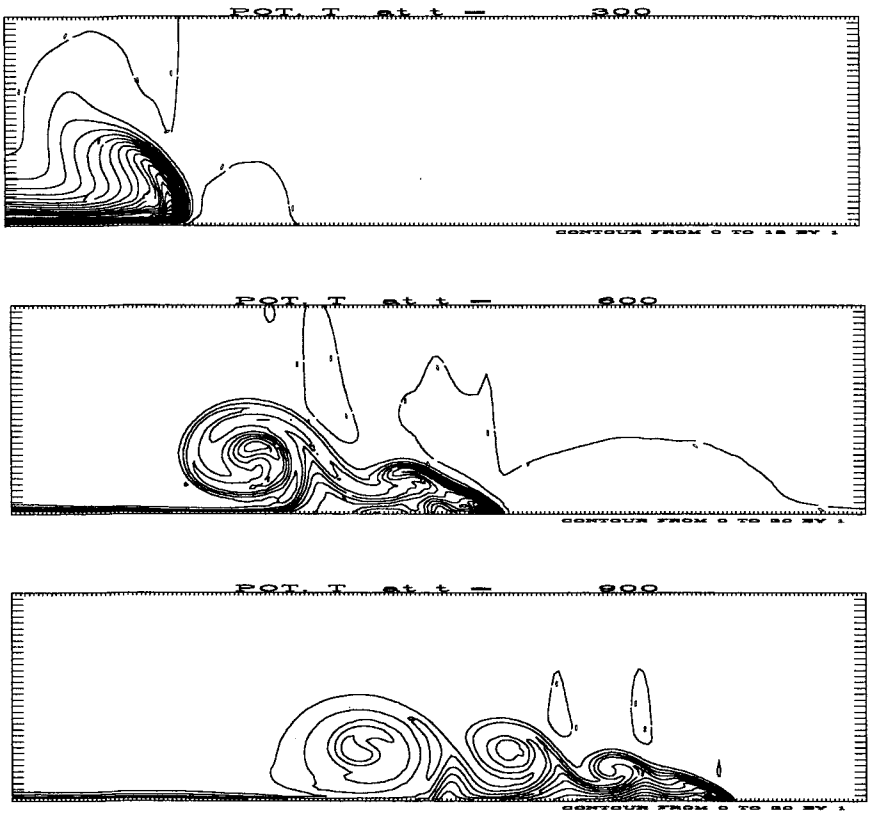

FIG. 1. The cold bubble test. Initial potential temperature and the potential temperatures after 300, 600, and 900 s in the right-hand part of the integration domain extending from the center to 19 200 m, and from the surface to 4600 m. The grid size is $\Delta z \approx \Delta x = 100$ m and $\Delta t = 0.3$ s. The contour interval is 1 K.

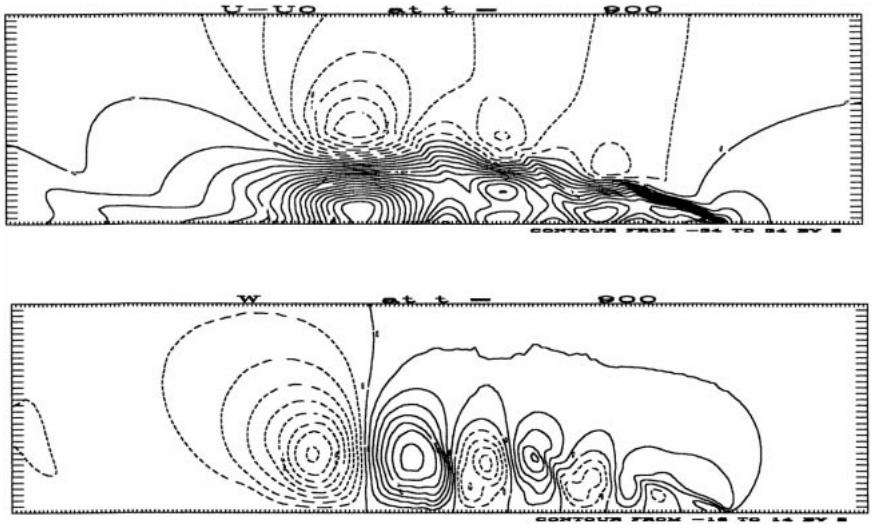

FIG. 2. The cold bubble test. The u component of wind (upper panel) and the w component of wind (lower panel) after 900 s in the right-hand part of the integration domain extending from the center to 19 200 m, and from the surface to 4600 m. The grid size is $\Delta z \approx \Delta x = 100$ m and $\Delta t = 0.3$ s. The contour interval is 2 m s^{-1}. The dashed contours indicate negative values.

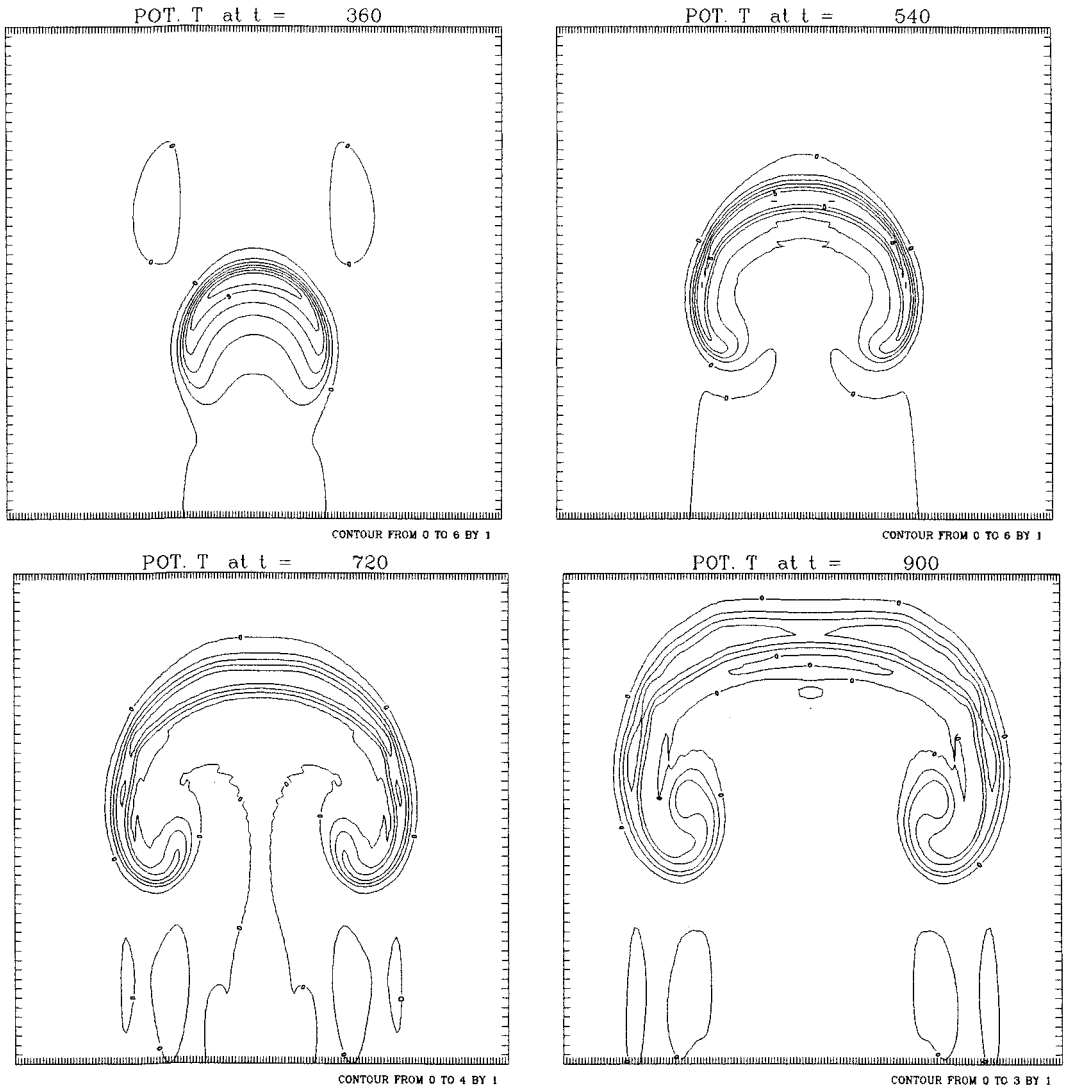

FIG. 3. The potential temperature deviation after 360, 540, 720, and 900 s (from upper left to lower right panel, respectively) in the warm bubble test. The area shown extends 16 km along the x axis, and from 0 to 13 200 m along the z axis. The contour interval is 1 K.

resolution was l00 m on the average. The time step with this spatial resolution was 0.3 s as before. The cyclic boundary conditions were prescribed. The divergence damping and time filtering were not used. The diffusion coefficients $K\Delta t/\Delta s^2$ along the x and σ axes were, respectively, 0.0015 and 0.0 for u, 0.0015 and 0.0015 for T, and 0.015 and 0.015 for w. As before, the three-point spatial filter with the coefficient wa = 0.15 was applied to ε_1 defined by (3.19).

The potential temperature deviation is presented after 360, 540, 720, and 900 s in Fig. 3. The area shown extends 16 km along the x axis, and from 1000 to 13 200 m along the z axis. The contour interval is 1 K. The rate of ascent and the intensity of the disturbance agree with those reported by Gallus and Rancic (1996). The low resolution test by Mendez-Nunez and Carroll (1994) can also be used for qualitative comparison.

c. The nonlinear mountain wave test

Xue et al. (1995) compared an analytical solution of the nonlinear mountain wave problem with the Boussinesq approximation and the numerical solution obtained with the version of the Advanced Regional Prediction System model using the Boussinesq approximation. The test reported here was made using the fully compressible model without any approximation, following as closely as possible the experiment of Xue et al. (1995). The height of the bell shaped hill was 500 m, and its half-width was 2000 m. The basic-state hori-

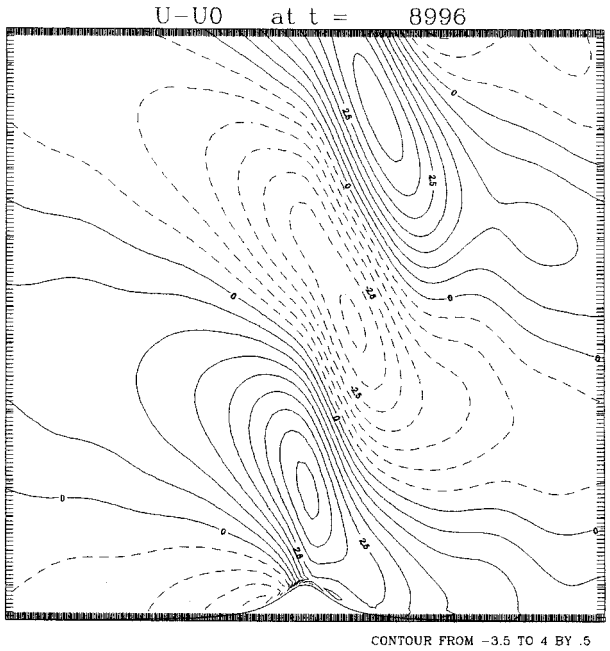

FIG. 4. The deviation of the horizontal wind from its basic-state uniform value (10 m s^{-1}) after 9000 s. The area shown extends 18 400 m on each side of the center of the mountain, and from 0 to 8000 m in the vertical. The contour interval is 0.5 m s^{-1} and the dashed contours indicate negative values.

zontal wind was 10 m s^{-1}, and the Brunt–Väisälä stability parameter N was approximately 0.01 s^{-1}. The horizontal grid size was 400 m covering a domain of about 145 km. The pressure at the top was 64 hPa, and the initial sea level pressure was 10^5 Pa. The height of the atmosphere of the model was about 17 500 m. The vertical coordinate used 143 layers of equal mass (constant $\Delta\sigma$), which provides about 125-m vertical spacing on the average. The time step was $\Delta t = 1.2$ s. The cyclic boundary conditions are used at the lateral boundaries. In the top part of the domain, the Rayleigh damping was applied with the weight proportional to the formula

$$\cos^2\left(\frac{\pi}{2}\frac{z_{\max} - z}{z_{\max} - z_c}\right) \quad \text{for } z > z_c, \tag{5.5}$$

where z is the height of the grid point. The maximum height $z_{\max}$ is equal to the height of the domain, and z_c was 9000 m. For the maximum height, the weight reaches the maximum of $0.001/\Delta t$. In addition, the Rayleigh damping was applied along the lateral boundaries as explained before. The horizontal divergence damping and time filtering were not used. The second-order diffusion coefficients $K\Delta t/\Delta s^2$ along the x and σ axes were, respectively, 0.005 and 0.0 for u, 0.007 and 0.0 for T, and 0.005 and 0.0 for w. As before, a centered three-point spatial filter with the coefficient $wa = 0.15$ was applied to ε_1 defined by (3.19).

The deviation of the horizontal wind from the basic state after 9000 s is shown in Fig. 4 with the contour interval of 0.5 m s^{-1}. The area shown extends 18 400 m on each side of the center of the mountain, and from 0 to 8000 m in the vertical. The qualitative and quantitative agreement with the analytical solution and the numerical solution discussed by Xue et al. (1995) are reasonably good considering the remaining differences between the tests. Note that in the test by Xue et al. (1995) the prognostic fields were initialized over a period of 1000 s.

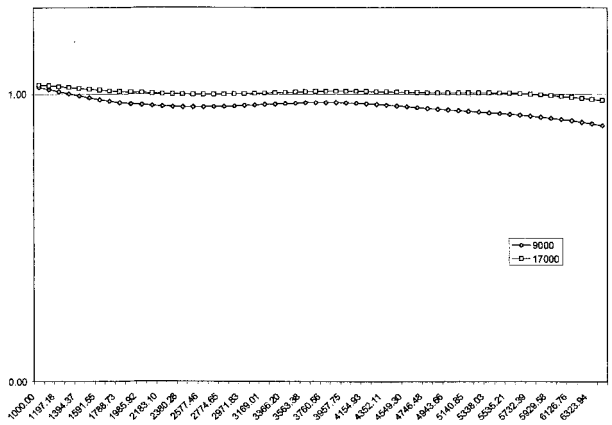

FIG. 5. The momentum flux normalized by its theoretical value. The height on the abscissa ranges from 1000 to 6400 m. The flux profiles after, respectively, 9000 and 17 000 s are marked by empty diamonds and empty squares.

The vertical momentum flux profiles normalized by the theoretical value of the flux (Xue et al. 1995) after 9000 and 17 000 s are shown in Fig. 5. The height is on the abscissa ranging from 1000 to 6400 m. The flux profiles after 9000 and 17 000 s are marked by empty diamonds and empty squares, respectively. As can be seen from the figure, after 9000 s the solution is rather close to the steady state. After 17 000 s, the normalized fluxes vary between 0.98 and 1.03.

6. Real data tests

The approach described in the previous sections has been implemented starting from the National Centers For Environmental Prediction Meso Eta Model. The details about the finite differencing schemes used in the model can be found in Janjic (1979, 1984, 1997), Janjic et al. (1995), and Mesinger et al. (1988). The model physics is discussed in Chen et al. (1997), Janjic (1990, 1994, 1996a,b), and Zhao and Carr (1997). The three-dimensional nonhydrostatic model dynamics and numerics agree to the maximum possible extent with those of the two-dimensional model used in the tests of the preceding section. The model appears to be computationally robust at all horizontal resolutions and efficient in NWP applications. The extra computational cost due to the nonhydrostatic extension is about 20% of that required by the hydrostatic dynamics, in terms of both computer time and memory.

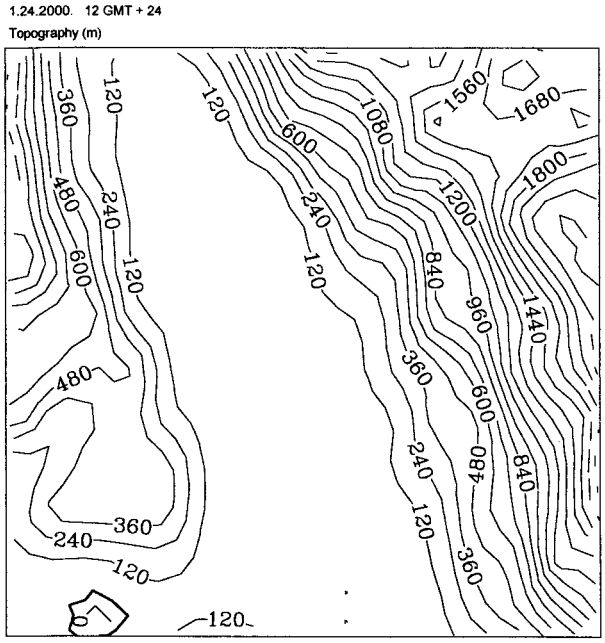

FIG. 6. The topography of the 2° by 2° region in California shown with 120-m contour interval.

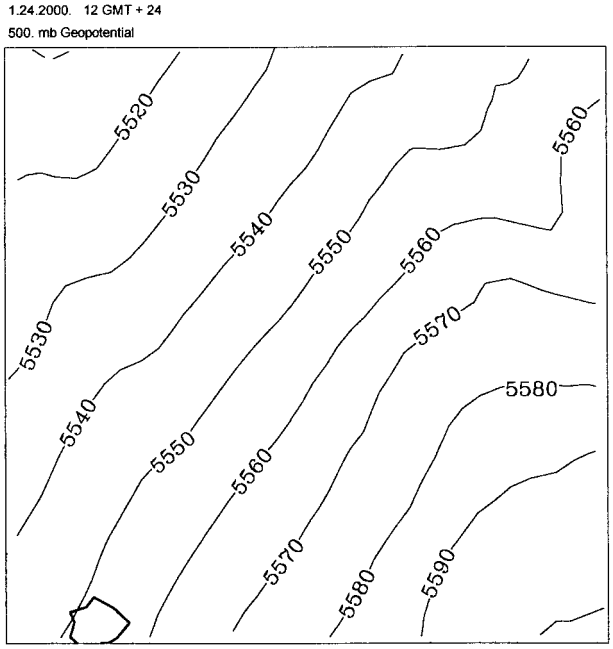

FIG. 7. The 24-h nonhydrostatic forecast of height at 500 hPa valid at 1200 UTC 25 Jan 2000. The contour interval is 10 m.

There is insufficient evidence concerning the impact of the nonhydrostatic dynamics on numerical weather forecasts using the horizontal resolutions of the order of 1–10 km. In order to elucidate this point a test was carried out with the horizontal resolution (i.e., the shortest distance between two grid points carrying the same variable) of about 8 km. Such a relatively coarse resolution was chosen because it was believed to be representative for the next generation of numerical weather prediction models that will be applied on continental and larger scales.

The model had 32 levels in the vertical and used the terrain-following σ vertical coordinate. In order to improve the accuracy of the pressure gradient force calculation, a scheme was used that reduces to the scheme proposed by Janjic (1977) (see also Janjic 1998) for the hydrostatic atmosphere. The model topography was defined in the most straightforward way, by bilinear interpolation of the 10-min U.S. Navy data. After the interpolation, one pass of five-point averaging was applied over the land points in order to eliminate the two-grid-interval wave in the terrain height, and thereby prevent the generation of small-scale noise by the mountains.

The case considered occurred in California between 1200 UTC 24 January 2000 and 1200 UTC 25 January 2000. The integration domain was 4° by 4° in the rotated latitude–longitude coordinate system with the coordinate origin located in the center of the domain. The topography of the 2° by 2° region in the middle of the integration domain is presented in Fig. 6 with a 120-m contour interval. The 24-h nonhydrostatic forecast of the 500-hPa height valid at 1200 UTC 25 January 2000 is shown in the same domain in Fig. 7 with a contour interval of 10 m. As can be seen from the figure, the flow aloft is southwesterly, forcing the moist maritime air to ascend over the steep mountain slopes.

The accumulated precipitation over the 24-h forecast period ending at 1200 UTC 25 January 2000 obtained using the nonhydrostatic model is shown in Fig. 8 only for the central 2° by 2° part of the integration domain. The contour interval is 10 mm. The precipitation amount at the maximum reaches about 180 mm. Almost all of the precipitation came from the grid-scale precipitation and not from the convection. The corresponding result for the hydrostatic run is shown in Fig. 9 using the same arrangement. As can be seen from the figure, the precipitation pattern remained generally similar to that from the nonhydrostatic run. However, differences in details are noticeable even at the horizontal resolution of 8 km. In particular, note the appearance of ''cut-off'' minima in the precipitation pattern located upstream with respect to the major maxima in the nonhydrostatic run. In order to check whether this feature was indeed an artifact of the nonhydrostatic dynamics, the test was repeated around one of these minima with approximately 1-km horizontal resolution and in a proportionally reduced integration domain. The precipitation forecasts obtained with the nonhydrostatic and the hydrostatic models in the middle quarter of the small domain are presented in Figs. 10 and 11, respectively, with 5-mm contour interval. As can be seen from the figures, the nonhydrostatic model again produced a cut-off minimum in the precipitation pattern in place of a trough in case of

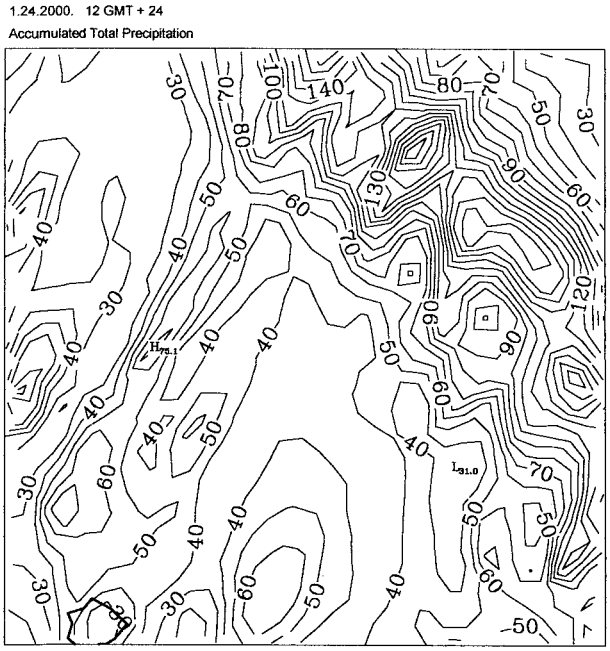

FIG. 8. Accumulated precipitation over the 24-h forecast period ending at 1200 UTC 25 Jan 2000 obtained using the nonhydrostatic model with 8-km resolution. The contour interval is 10 mm.

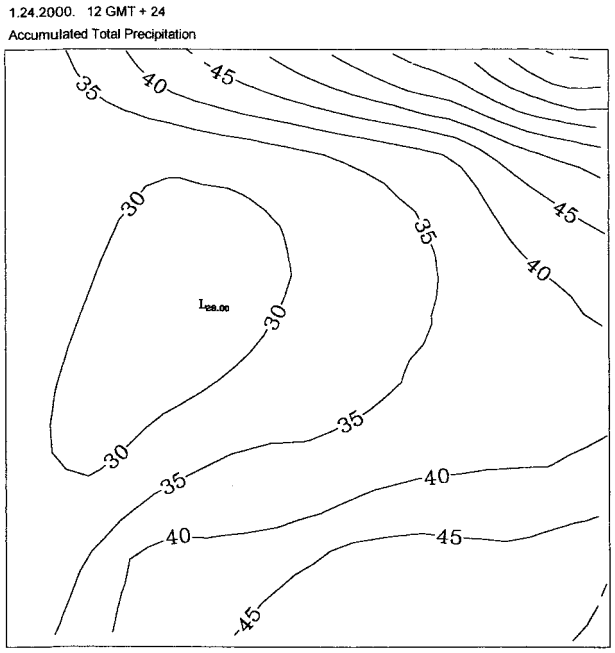

FIG. 10. Accumulated precipitation over the 24-h forecast period ending at 1200 UTC 25 Jan 2000 obtained using the nonhydrostatic model with 1-km resolution. The contour interval is 5 mm.

the hydrostatic model. Understandably, the precipitation amounts in the 1- and the 8-km runs do not coincide.

The 24-h forecast of the nonhydrostatic pressure at the 700-hPa hydrostatic pressure level obtained in the 8-km nonhydrostatic run is shown in Fig. 12 in the same 2° by 2° area as before with the contour interval of 1 Pa. As can be seen from the figure, the nonhydrostatic deviation can reach a fraction of 1 hPa, which agrees with theoretical estimates. Although these deviations are small, their contributions to the local values of the pres-

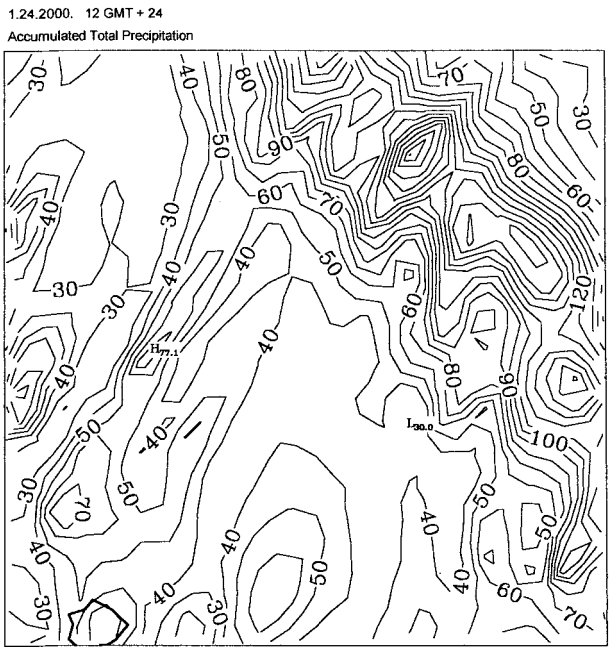

FIG. 9. Accumulated precipitation over the 24-h forecast period ending at 1200 UTC 25 Jan 2000 obtained using the hydrostatic model with 8-km resolution. The contour interval is 10 mm.

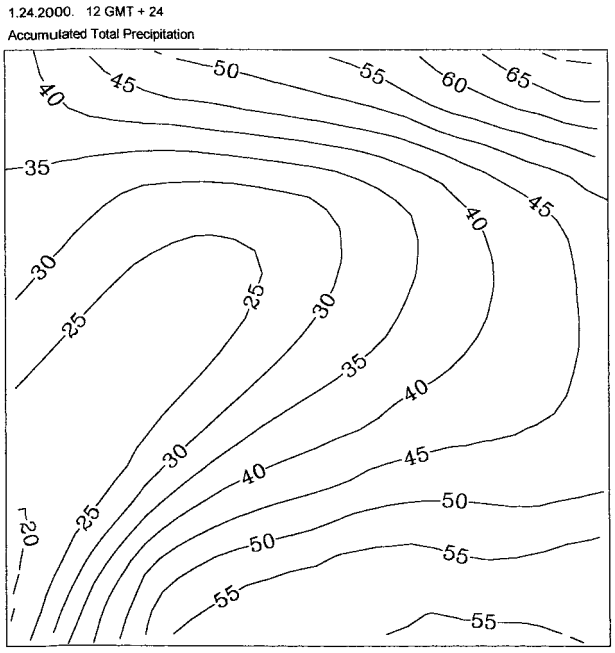

FIG. 11. Accumulated precipitation over the 24-h forecast period ending at 1200 UTC 25 Jan 2000 obtained using the hydrostatic model with 1-km resolution. The contour interval is 5 mm.

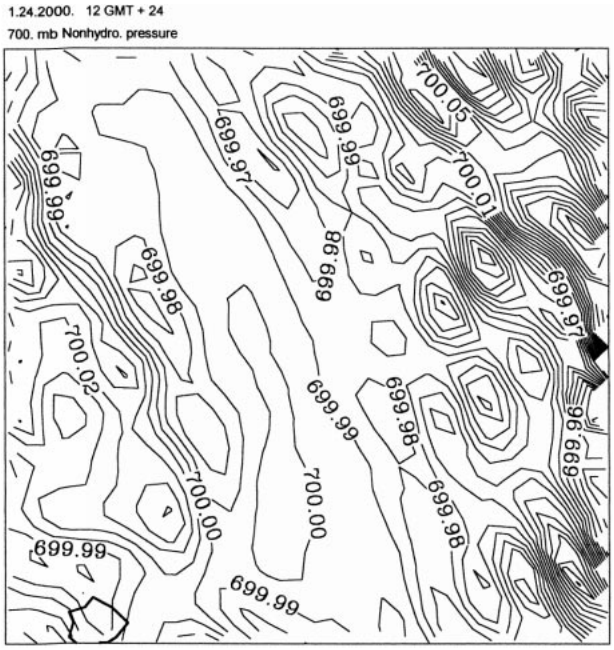

FIG. 12. The 24-h forecast of the nonhydrostatic pressure at the 700-hPa hydrostatic pressure level valid at 1200 UTC 25 Jan 2000. The contour interval is 1 Pa.

sure gradient force are comparable in magnitude with the synoptic-scale contributions and presumably affect the small-scale circulations significantly.

It should be reiterated that the proposed approach has demonstrated a good computational efficiency in NWP applications. For example, with 4-km grid size, 41 by 81 grid points in the horizontal, 32 levels in the vertical, and 10-s time step, the 24-h nonhydrostatic forecast takes slightly over 7½ h on a single processor 450 mHz Pentium II personal computer. The forecast with exactly the same setup, but with the nonhydrostatic extension switched off, takes slightly less than 6½ h.

7. Conclusions

Instead of extending mesoscale nonhydrostatic modeling concepts to the synoptic scales, a hydrostatic NWP model using the mass-based σ vertical coordinate has been extended to include the nonhydrostatic motions, preserving the favorable features of the hydrostatic formulation. Nonhydrostatic model obtained in this way represents a natural, evolutionary extension of the hydrostatic model. The equations solved are equivalent to those discussed by Laprise (1992).

The basic idea applied was to split the system of the nonhydrostatic equations into two parts: (a) the part that corresponds basically to the hydrostatic system, except for higher-order corrections due to the vertical acceleration, and (b) the system of equations that allows computation of the corrections appearing in the first system due to the vertical acceleration. This procedure does not require linearization or approximation of any kind.

The nonhydrostatic dynamics is introduced through an add-on nonhydrostatic module. The separation of the nonhydrostatic contributions shows in a transparent way where, how, and to what extent relaxing the hydrostatic approximation affects the familiar hydrostatic equations. The nonhydrostatic module can be turned on and off depending on resolution, so that the same model can be run in the hydrostatic mode at lower resolutions with no extra cost. This also allows easy comparison of hydrostatic and nonhydrostatic solutions of otherwise identical models.

The proposed nonhydrostatic model appears to be computationally robust and efficient in NWP applications. With the current coding, the extra computational cost due to the nonhydrostatic extension is of the order of 20% of that required by the hydrostatic dynamics, both in terms of computer time and memory. The relatively low cost of the nonhydrostatic dynamics justifies the application of the nonhydrostatic model even at medium resolutions. Compared to the hydrostatic version of the model, no additional computational boundary conditions were needed in real data runs.

At lower resolutions, in the hydrostatic limit, the forecasts of traditional meteorological parameters obtained using the hydrostatic and the nonhydrostatic model are almost indistinguishable. The model also demonstrated the presence of important two-dimensional nonhydrostatic effects at very high resolutions. At these scales, the hydrostatic and the nonhydrostatic solutions were substantially different. The nonhydrostatic model was generally more robust than the hydrostatic one and produced smoother solutions.

The impact of the nonhydrostatic dynamics appears to be weak at the horizontal resolutions of about 8 km. However, a visible effect on the orographic precipitation was detected. In addition, the nonhydrostatic deviation of pressure made a significant small-scale contribution to the pressure gradient force at places.

The proposed approach appears well suited for models designed for a wide range of horizontal resolutions, and in particular for unified global and regional forecasting systems. Being developed from an existing model, the new model requires only minimal changes of the existing preprocessing and postprocessing infrastructure.

Acknowledgments. The authors are indebted to Mr. Dusan Jovic for his help in developing a workstation version of the model and handling the graphics. The help of Dr. Thomas L. Black of NCEP and Dr. William Gallus of Iowa State University in the early stages of testing the system was invaluable. The understanding and support that this research received from Drs. Geoff DiMego, Eugenia Kalnay, and Steve Lord of NCEP have been essential for its successful completion. Thanks are also due to Prof. George Kallos of the Uni-

versity of Athens for providing the facilities and assistance used at an early stage of testing of the workstation version of the model. Numerous discussions with Dr. Joe Klemp of NCAR influenced the course of this research. Dr. William Collins of NCEP graciously shared his expertise on the problem of the formation of contrary flow in the lee of mountains. The authors are also grateful to many other persons from NCEP and NCAR who have provided assistance during this work.

This research was conducted, in part, in response to requirements and funding by the Federal Aviation Administration (FAA). The views expressed are those of the authors and do not necessarily represent the official policy or position of the FAA.

REFERENCES

Ames, W. F., 1969: *Numerical Methods for Partial Differential Equations.* Nelson, 291 pp.

Bubnova, R., G. Hello, P. Benard, and J.-F. Geleyn, 1995: Integration of the fully elastic equations cast in the hydrostatic pressure terrain-following coordinate in the framework of the ARPEGE/Aladin NWP system. *Mon. Wea. Rev.,* **123,** 515–535.

Chen, F., Z. Janjic, and K. Mitchell, 1997: Impact of atmospheric surface-layer parameterization in the new land-surface scheme of the NCEP mesoscale Eta model. *Bound.-Layer Meteor.,* **48,** 391–421.

Davies, H. C., 1976: A lateral boundary formulation for multi-level prediction models. *Quart. J. Roy. Meteor. Soc.,* **102,** 405–418.

Drogemeier, K. K., 1985: The numerical simulation of thunderstorm outflow dynamics. Ph.D. dissertation, University of Illinois at Urbana–Champaign, 695 pp.

Gadd, A. J., 1974: An economical explicit integration scheme. Met. Office Tech. Note 44, 7 pp. [Available from The Met. Office, London Road, Bracknell, Berkshire RG12 2SZ, United Kingdom.]

Gallus, W. A., and M. Rancic, 1996: A non-hydrostatic version of the NMC's regional Eta model. *Quart. J. Roy. Meteor. Soc.,* **122,** 495–513.

Janjic, T. Z., 1998: Comments on ''A finite-volume integration method for computing pressure gradient force in general vertical coordinates'' by Shian-Jiann Lin (July B, 1997, **123,** 1749–1762). *Quart. J. Roy. Meteor. Soc.,* **124,** 2527–2529.

Janjic, Z. I., 1977: Pressure gradient force and advection scheme used for forecasting with steep and small scale topography. *Contrib. Atmos. Phys.,* **50,** 186–199.

——, 1979: Forward-backward scheme modified to prevent two-grid-interval noise and its application in sigma coordinate models. *Contrib. Atmos. Phys.,* **52,** 69–84.

——, 1984: Non-linear advection schemes and energy cascade on semi-staggered grids. *Mon. Wea. Rev.,* **112,** 1234–1245.

——, 1990: The step-mountain coordinate: Physical package. *Mon. Wea. Rev.,* **118,** 1429–1443.

——, 1994: The step-mountain eta coordinate model: Further developments of the convection, viscous sublayer, and turbulence closure schemes. *Mon. Wea. Rev.,* **122,** 927–945.

——, 1996a: The Mellor–Yamada level 2.5 scheme in the NCEP Eta model. Preprints, *11th Conf. on Numerical Weather Prediction,* Norfolk, VA, Amer. Meteor. Soc., 333–334.

——, 1996b: The surface layer in the NCEP Eta model. Preprints, *11th Conf. on Numerical Weather Prediction,* Norfolk, VA, Amer. Meteor. Soc., 354–355.

——, 1997: Advection scheme for passive substances in the NCEP Eta model. *Research Activities in Atmospheric and Oceanic Modelling,* WMO, 3.14.

——, and A. Wiin-Nielsen, 1977: On geostrophic adjustment and numerical procedures in a rotating fluid. *J. Atmos. Sci.,* **34,** 297–310.

——, F. Mesinger, and T. L. Black, 1995: The pressure advection term and additive splitting in split-explicit models. *Quart. J. Roy. Meteor. Soc.,* **121,** 953–957.

Laprise, R., 1992: The Euler equations of motion with hydrostatic pressure as an independent variable. *Mon. Wea. Rev.,* **120,** 197–207.

Mendez-Nunez, L. R., and J. J. Carroll, 1994: Application of the MacCormack scheme to atmospheric nonhydrostatic models. *Mon. Wea. Rev.,* **122,** 984–1000.

Mesinger, F., Z. I. Janjic, S. Nickovic, D. Gavrilov, and D. G. Deaven, 1988: The step-mountain coordinate: Model description and performance for cases of Alpine lee cyclogenesis and for a case of an Appalachian redevelopment. *Mon. Wea. Rev.,* **116,** 1493–1518.

Straka, J. M., R. B. Wilhelmson, L. J. Wicker, J. R. Anderson, and K. K. Droegemeier, 1993: Numerical solutions of a non-linear density current: a benchmark solution and comparisons. *Int. J. Numer. Meth. Fluids,* **17,** 1–22.

Xue, M., K. K. Drogemeier, V. Wong, A. Shapiro, and K. Brewster, 1995: Advanced Regional Prediction System. ARPS Version 4.0 User's Guide, Center for Analysis and Prediction of Storms, National Science Foundation, Federal Aviation Administration, The University of Oklahoma, 380 pp.

Zhao, Q., and F. H. Carr, 1997: A prognostic cloud scheme for operational NWP models. *Mon. Wea. Rev.,* **125,** 1931–1953.